Singular orientations and faceted motion of dislocations in body-centered cubic crystals

Keonwook Kang[a,1], Vasily V. Bulatov[b], and Wei Cai[a,2]

[a]Department of Mechanical Engineering, Stanford University, Stanford, CA 94305; and [b]Lawrence Livermore National Laboratory, Livermore, CA 94550

Edited by William D. Nix, Stanford University, Stanford, CA, and approved August 7, 2012 (received for review April 12, 2012)

Dislocation mobility is a fundamental material property that controls strength and ductility of crystals. An important measure of dislocation mobility is its Peierls stress, i.e., the minimal stress required to move a dislocation at zero temperature. Here we report that, in the body-centered cubic metal tantalum, the Peierls stress as a function of dislocation orientation exhibits fine structure with several singular orientations of high Peierls stress—stress spikes—surrounded by vicinal plateau regions. While the classical Peierls-Nabarro model captures the high Peierls stress of singular orientations, an extension that allows dislocations to bend is necessary to account for the plateau regions. Our results clarify the notion of dislocation kinks as meaningful only for orientations within the plateau regions vicinal to the Peierls stress spikes. These observations lead us to propose a Read-Shockley type classification of dislocation orientations into three distinct classes—special, vicinal, and general—with respect to their Peierls stress and motion mechanisms. We predict that dislocation loops expanding under stress at sufficiently low temperatures, should develop well defined facets corresponding to two special orientations of highest Peierls stress, the screw and the M111 orientations, both moving by kink mechanism. We propose that both the screw and the M111 dislocations are jointly responsible for the yield behavior of BCC metals at low temperatures.

metal plasticity | thermally activated motion | anisotropic mobility | molecular statics | molecular dynamics

Strength, formability, toughness, and other important properties of metals and alloys are largely defined by the ability of special crystal defects—dislocations—to move in response to stress. Crystal dislocations were first proposed in 1934 (1–3) to explain a large discrepancy between the measured yield strength and the expected (ideal) shear strength of a perfect crystal. The key idea was that the stress it takes to move a dislocation must be significantly lower than is necessary to make the atomic planes slide against each other in a perfect crystal (4). The concept of Peierls stress (PS), defined as the minimal stress necessary to move a dislocation at zero temperature, has played a prominent role in dislocation physics and crystal plasticity. The specific value of the PS in a given material is believed to delineate two distinctly different regimes of dislocation motion (5). At a stress below PS dislocation motion requires thermal assistance and proceeds via kink-pair nucleation and migration. In contrast, at a stress above PS thermal assistance is no longer necessary and dislocation's mobility is limited by its interaction with phonons and electrons. Similar to other extended crystal defects; e.g., grain boundaries, the mobility of a given dislocation is known to depend on its orientation in the host crystal, however the nature of such mobility anisotropy and its effect on crystal plasticity are neither understood nor quantified.

Here we use atomistic calculations to carefully examine variations in the PS values over the entire range of dislocation orientations in the {110} close packed planes of the body-centered cubic (BCC) metal tantalum (Ta). The observed PS variations are striking (Fig. 1) and can not be fully explained within existing theory. However we show that an extension of the classical Peierls-Nabarro (PN) model offers a semiquantitative description of the observed PS variations, provided the dislocation lines are allowed to bend. Our analysis clarifies the notion of dislocation kinks as meaningful and constructive only for vicinal orientations surrounding the singular PS spikes leading us to propose a dislocation line classification of the Read-Shockley type (6). Two of the singular orientations stand out by their high PS magnitudes: the screw orientation in which the line is at 0° to its Burgers vector and the M111 orientation at 71° to the Burgers vector. Focusing attention on these two singular orientations, we present strong evidence from atomistic calculations suggesting that at sufficiently low temperatures both the screw and the M111 dislocations move by kink mechanisms. This suggestion is contrary to the pervasive notion that in BCC metals only the screw dislocations experience high lattice resistance to their motion whereas all nonscrew dislocations are qualitatively the same and can be well represented by fast moving orientations close to 90° (edges). To clarify the effects of the low M111 mobility on crystal plasticity we use Dislocation Dynamics (DD) simulations in which dislocation mobility function is anisotropic and contains two slow orientations—screw and M111. The DD results suggest that low mobility of the second slowest orientation (M111) results in dynamic faceting of dislocation loops expanding in the {110} glide planes. The same low mobility defines the rate at which dislocation loops sweep the area and may be responsible for yield behavior observed in BCC metals at low temperatures.

Results

To examine the anisotropy of dislocation mobility we computed PS for 87 different orientations of $\mathbf{b} = \frac{1}{2}[111]$ dislocations in the $(1\bar{1}0)$ slip plane of a BCC crystal using the Finnis-Sinclair interatomic potential model for Ta (7). Several methods were employed specifically to minimize numerical errors in PS calculations (see *Materials and Methods*). The remaining errors depend on the orientation and are estimated to be within 3 MPa for 73 out of 87 orientations and within 7 MPa for all 87 orientations.

In Fig. 1 the computed PS is plotted against the character angle θ; i.e., the angle between the dislocation line and its Burgers vector. Perhaps the most prominent feature on the plot is the PS spikes at several low-index orientations. The highest of the spikes corresponds to the screw ($\theta = 0°$, or [111]) orientation, at $\tau_P = 2{,}785$ MPa. The second highest spike of 547 MPa is at the mixed $[11\bar{1}]$ orientation ($\theta = 70.53°$), labelled here as M111 (8). Other, less prominent, spikes are observed for a few other low-index orientations, such as [110] and [001], with PS between 100 and 200 MPa. At some higher index directions still lower spikes are detectable; e.g., [112], [113], [221], and [331], with PS between 50 and 100 MPa. The remaining orientations constitute a large

Author contributions: K.K., V.V.B., and W.C. designed research, performed research, analyzed data, and wrote the paper.

The authors declare no conflict of interest.

This article is a PNAS Direct Submission.

[1]Present address: Theoretical Division, Los Alamos National Laboratory, Los Alamos, NM 87545.

[2]To whom correspondence should be addressed. E-mail: caiwei@stanford.edu.

This article contains supporting information online at www.pnas.org/lookup/suppl/doi:10.1073/pnas.1206079109/-/DCSupplemental.

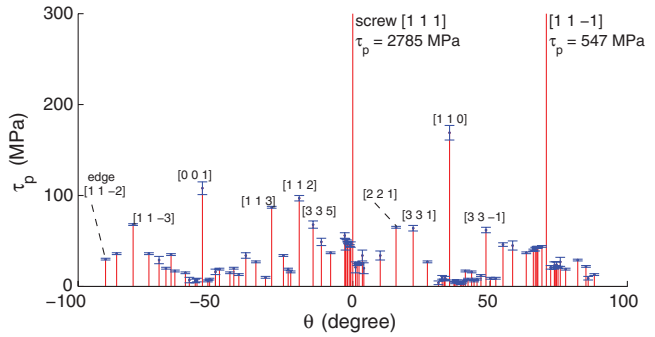

Fig. 1. Atomistically computed Peierls stress of dislocations with Burgers vector $\mathbf{b} = \frac{1}{2}[111]$ as a function of dislocation character angle θ on the $(1\bar{1}0)$ plane in BCC Ta.

background group of orientations with PS values ranging from 3 to 50 MPa. Still finer details may be seen within this background group but their significance remains uncertain due to the finite accuracy of our calculations. When scaled by the shear modulus of Ta, our six highest PS spikes are comparable to the PS values reported earlier for the same six low-index orientations in model BCC crystals (9), suggesting that the existence of such singularities is a consequence of BCC lattice geometry.

To rationalize our findings we first appeal to the classical Peierls-Nabarro (PN) model of dislocations. Remarkable in its simplicity and clarity, the PN model is a hybrid approach that reproduces the long-ranged elastic distortions caused by the dislocation while, at the same time, capturing the essential nonlinear effects in the atomic core (10, 11). Key for our discussion here is that the PN model predicts the magnitude of PS τ_P to depend exponentially on the ratio of the dislocation core width w_{PN} to the spacing a between the neighboring Peierls valleys (minimum energy line positions in the glide plane). In the relevant limit of $w_{PN} > a$ (12),

$$\frac{\tau_P}{\tau_{max}} \approx 4\pi \frac{w_{PN}}{a} \exp\left(-2\pi \frac{w_{PN}}{a}\right), \qquad [1]$$

where τ_{max} is the ideal shear strength for the slip along [111] direction in the $(1\bar{1}0)$ plane *. $w_{PN} = [\cos^2\theta + \sin^2\theta/(1-\nu)]\frac{b}{4\pi}\frac{\mu}{\tau_{max}}$, where μ is the shear modulus, ν is the Poisson ratio, and b is the magnitude of the Burgers vector. For the model potential used here, $\tau_{max} = 10.5$ GPa. Whereas the core width w_{PN} varies only modestly within the $(1\bar{1}0)$ plane, spacing a ranges from the maximum $\sqrt{2/3}a_0$ for [111] and $[11\bar{1}]$ orientations (here a_0 is the lattice constant) to nearly zero for high index orientations. In fact, when considered as functions of θ, both a and τ_P (as predicted by Eq. **1**) are examples of the Dirichlet function (13) that is equal to zero for any irrational orientation while taking on finite values for all rational orientations.

Fig. 2 *A* and *B* compare the atomistic PS values against τ_P computed from Eq. **1** of the PN model. It turns out that the very low-index orientations that display the highest values of PS in the atomistic calculations, also possess the smallest w_{PN}/a ratios resulting in the highest PS as predicted by the PN model (Eq. **1**). For the [111] (screw) orientation, the atomistic value of 2,785 MPa is remarkably close the PN prediction of 2,650 MPa. This agreement may be considered fortuitous given that the equilibrium core structure of screw dislocations in BCC metals does not spread out on one particular plane, contrary to the assumption made in the PN model. For the $[11\bar{1}]$ (M111) orientation with the second smallest w_{PN}/a ratio, the PN model predicts the second highest value of PS, again in agreement with the atomistic

*τ_{max} is the maximum derivative of the misfit potential with respect to the inter-planar displacement in the slip direction (39).

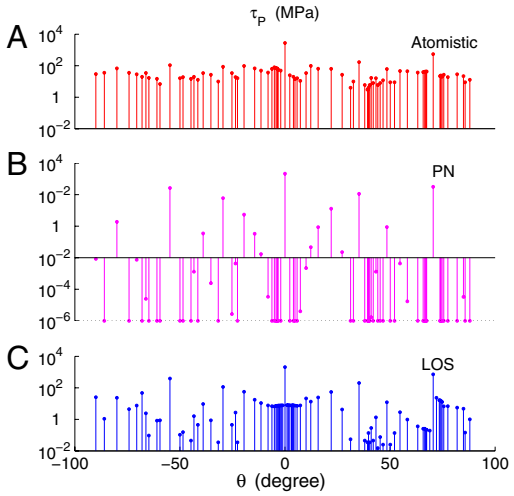

Fig. 2. Semilog plot of the Peierls stress as a function of the character angle θ: (*A*) the results of atomistic calculations, (*B*) predictions of the PN theory, and (*C*) the LOS model predictions. In (*B*), the PS values below 10^{-6} MPa are truncated for clarity.

result. This trend holds for a few more low-index orientations with small w_{PN}/a ratios supporting our assertion that the existence of orientations with high PS is largely a geometric effect (see also ref. (14) reporting similar observations for γ-TiAl with $L1_0$ structure). However, for higher w_{PN}/a ratio, the PN model disagrees strongly with our atomistic results. For example, in the angular range of $|\theta| < 4°$ around the screw orientation, the PN model predicts τ_P to fall below 10^{-10} MPa whereas all atomistic PS values within the same range are reliably above 10 MPa. In fact, the atomistic PS stays above 10 MPa for more than 75% of the orientations considered in this study, and no single atomistic PS value falls below a *floor* of 3 MPa. In contrast, in the PN model only eight orientations have the PS above 1 MPa, and many of the others fall below 10^{-6} MPa and had to be truncated in Fig. 2*B*.

The Line-On-Substrate Model. To remedy the above mentioned shortcoming of the PN theory, here we consider a "line-on-substrate" (LOS) model that regards the dislocation as a line resting on a periodic energy landscape (substrate) representing the coupling between the dislocation line and the crystal lattice †. As shown in Fig. 3, the dislocation consists of line segments connecting nodes regularly spaced along horizontal axis z. Within the LOS model the dislocation enthalpy is

$$E(\{x_i\}) = E_{MSFT}(\{x_i\}) + \sum_i E_{LT}(\theta_{i,i+1}) \cdot L_{i,i+1} - \sigma b \cdot \Delta z \cdot \sum_i x_i, \qquad [2]$$

where the first term on the right hand side is constructed from the *misfit* energy in the PN model (12) and represents the interaction between the line and the substrate. The second term is a discretized *line tension* approximation (15, 16) to the elastic self energy that causes the dislocation to resist bending. The third term is the work done by the applied stress with the minus sign. The variables $\theta_{i,i+1}$, $L_{i,i+1}$, b, and Δz are defined in Fig. 3. The optimal shape of the line on the substrate is obtained by minimizing the enthalpy (Eq. **2**) with respect to the nodal positions x_i. The PS is defined as the lowest stress σ for which the minimization fails to converge.

In the limit of infinite bending stiffness $E_{LT} \to \infty$, the large line tension term forces the dislocation to remain perfectly

†This model is hinted at on pp. 257–258 in (5).

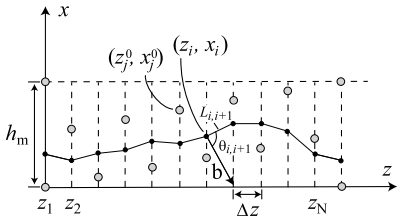

Fig. 3. Schematic of the LOS model. The black dots (z_i, x_i) connected by straight segments are the discretization nodes on the dislocation line. $L_{i,i+1}$ is the length of the segment connecting nodes i and $i+1$, and $\theta_{i,i+1}$ is the angle between this segment and the Burgers vector b. The gray circles (z_i^0, x_i^0) mark atomic positions on the $(1\bar{1}0)$ plane in an ideal (reference) BCC crystal. h_m is the spacing of atoms in the x direction, and Δz is the spacing between the lattice planes normal to the line axis z. Periodic boundary conditions are applied along z axis.

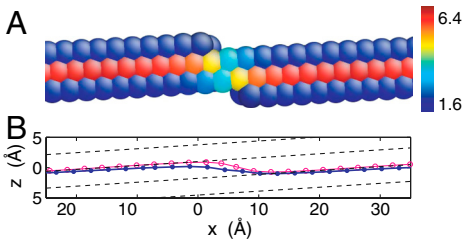

Fig. 4. (*A*) Atoms in the core of the dislocation with $[77\bar{8}]$ average orientation. Atoms are colored according to the centro-symmetry deviation (CSD) parameter. Only the atoms whose CSD exceeds 1.6 Å^2 are plotted. (*B*) The thin line (with circles) is the LOS model prediction for the equilibrium line shape of the same $[77\bar{8}]$ dislocation. The thick line (with dots) shows the shape of this dislocation extracted from the analysis of the atomistic configuration. The dashed lines indicate the location of the Peierls valleys along the $[11\bar{1}]$ orientation.

straight; in this limit the LOS model reduces to the PN model (12). Remarkably, just by admitting a finite line stiffness, the LOS model overcomes the principal shortcoming of the PN model that predicts vanishing PS in the limit of $w_{PN}/a \to \infty$. Furthermore, the LOS model qualitatively captures all the essential features of PS variations revealed in our atomistic calculations, as shown in Fig. 2*C*. In particular, for the low index orientations such as [111], $[11\bar{1}]$, [110], and [001], the LOS model predicts high PS values nearly identical to the PN model, suggesting that allowing the dislocation to bend is not essential for these orientations. However, for the higher index orientations where the PN model predicts vanishing Peierls stresses, the LOS model remains in qualitative agreement with the atomistic data. Furthermore, for orientations vicinal to screw and M111, the LOS model predict plateaus in the PS values, again in agreement with the atomistic calculations (compare Fig. 2 *A* and *C* near $\theta = 0°$ and $\theta = 71°$).

Stress Plateau and Kinks. The only difference between the PN model and the LOS model is that in the latter dislocations are allowed to bend to reduce their energy. Because the PS plateaus are reproduced in the LOS model but not in the PN model, the very existence of the PS plateaus must be due to dislocation bending. Fig. 4*B* shows the shape of a dislocation with an average $[77\bar{8}]$ orientation that minimizes the dislocation's energy as defined in the LOS model (Eq. **2**). The dislocation is seen to align along the $[11\bar{1}]$ orientation over most of its length while its average $[77\bar{8}]$ orientation is maintained by bending the line within a localized region, a kink. If the applied stress exceeds its PS, this dislocation moves by lateral motion of the kink along the line. This behavior explains the existence of the PS plateau around the $[11\bar{1}]$ orientation—in the angular range where the kink is well defined, the PS of a vicinal dislocation is the PS of the kink.

It is of interest to compare the shape of the $[77\bar{8}]$ line as predicted by the LOS model with the shape of the same orientation obtained in the atomistic model of Ta. To enable the comparison, we slice the atomic structure containing a fully relaxed $[77\bar{8}]$ dislocation into thin slabs normal to the $[11\bar{1}]$ direction. For each slab, the position of the dislocation center is obtained by matching the displacements of atoms within the slab to the displacement field of a straight Volterra dislocation (5). The dislocation centers for each slab are then connected by straight segments to depict the overall shape of the dislocation line. As shown in Fig. 4*B*, the line shape extracted from the atomistic configuration and that predicted by the LOS model are strikingly similar, confirming the usefulness of the LOS model for qualitative analysis of dislocation shapes and PS.

The concept of kinks is pervasive in physics but, in the specific context of dislocations in crystals, what constitutes a kink is still open to interpretation. Confusion stems, in part, from the lattice geometry itself where all but a few shortest lattice vectors can be regarded as sums of two other lattice vectors with lower Miller indices. Of these two vectors, the shorter one can be thought of as a kink. But does this observation mean that every high index dislocation orientation must contain kinks? Limited resolution of methods employed to visualize crystal defects can add to confusion. A representative example is given in Fig. 4*A*, where only the atoms in the dislocation core are plotted. These atoms appear to contain a sharp bend that is tempting to interpret as a kink. However, both appearance and positions of such a bend depend on a particular choice of a local measure of atom "defectiveness". For example, shown in Fig. 4*A* are only the "core" atoms whose centro-symmetry deviation (CSD) parameter (17) exceeds the threshold of 1.6 Å^2. Given the variety of per-atom measures proposed in the literature (17–20), our choice for CSD and its particular threshold value was largely arbitrary.

In the past, similar analyses have lead to claims (by ourselves included) that edge dislocations in BCC metals contain kinks (21–23). However, given the unwanted freedom in defining what constitutes a kink, such definitions are next to meaningless. We believe that it is only useful and constructive to invoke kinks to describe dislocations in an angular range $\Delta\theta$ of orientations around a singular PS spike where PS exhibits a plateau. Only for such orientations, the kink becomes a defined object possessing its own properties such as PS and width. Following (24) we estimate that $\Delta\theta \sim \sqrt{a^s \tau_P^s/(\mu b)}$, where τ_P^s is the PS and a^s is the spacing between neighboring Peierls valleys for the singular orientation. Fig. 1 suggests that the screw and the M111 orientations support kinks as well as, possibly, [110] and [001] orientations. However, the lower the PS of the singular orientation, the narrower the angular range $\Delta\theta$ in which the kinks can be identified. Furthermore, even when kinks are detectable in atomistic calculations, they can be washed out by line vibrations at finite temperatures or quantum zero-point vibrations, unless the PS of the singular orientation is sufficiently high.

What we observe here is quite similar to the Read-Shockley model (6) of grain boundaries, in which lattice misorientations are accommodated by geometrically necessary dislocations. Exploring this analogy, we classify dislocation line orientations in BCC metals as special (singular), vicinal, and general. Small (vicinal) deviations from a special orientation are accommodated by geometrically necessary kinks. However, unlike grain boundaries, special dislocation orientations are identified here not by the energy cusps, but by PS spikes instead.

Dislocation Mobility. The existence of well defined vicinal ranges around the screw and the M111 orientations suggests that both dislocations can move by kink mechanisms. Indeed, it is widely accepted that under certain conditions kink mechanisms define the motion of screw dislocations in BCC metals (25). To test the hypothesis that M111 dislocations also move by kink mechanisms, we performed molecular dynamics (MD) simulations over a

range of temperatures and stress (see *Materials and Methods*). Fig. 5*A* shows that, when plotted as a function of stress, the velocity of the M111 dislocation is S-shaped at temperatures below 200 K. This mobility behavior is similar to that of screw dislocations reported earlier (26). This comparison is a still stronger indication that, just like for the screws, thermal activation is required for the M111 dislocations to move under stress below the PS. Detailed analyses of dislocation trajectories confirm that under low stress/temperature conditions, the M111 dislocations move in a stop-and-go fashion where every unit translation is initiated by kink pair nucleation and spreading along the line, similar to the screw dislocations (26). Our observations of low mobility of M111 dislocations are supported by recent MD simulations of dislocation motion in iron (27).

When dislocation mobility is controlled by kink-pair mechanisms, the lower the temperature the higher the stress required to make the dislocation move at a given velocity. To quantify this effect, Fig. 5*B* plots several temperature-stress combinations that were found to maintain dislocation velocity at about 10 m·s^{-1}. At this velocity, we have found (empirically) that the dislocation moves by the kink mechanism. The line connecting the data points thus delineates the thermally activated regime from the drag-controlled regime of dislocation motion: under the temperature-stress conditions within the shaded area, the M111 dislocation is expected to move by kink mechanisms (if it moves at all).

The singular character of the M111 dislocations can have experimentally detectable consequences. To better understand what role the M111 dislocations can play in crystal plasticity, we performed MD and DD simulations of a glide dislocation loop expanding on the {110} slip plane. In our DD simulations, mobility of dislocation segments comprising the loop was anisotropic. Expressed as a function of the segment character angle θ the mobility was assumed to have two cusps: the deepest cusp at the screw orientation ($\theta = 0°$) and the second cusp at the M111 orientation ($\theta = 70.5°$) (see Fig. 6*B*). For simplicity, an idealized linear mobility law is assumed in this simulation, but qualitatively the same behavior is observed in DD simulations using more complex and realistic mobility laws (see *SI Text*). As the initially circular loop expands under the applied stress, it gradually develops a shape of rounded parallelogram bounded by four dislocation segments of the two slowest-moving orientations, as shown in Fig. 6*A*. Similar behavior is found in the MD snapshot shown in Fig. 6*C*. This faceting behavior is in close analogy to crystal growth where, at the initial stages of growth, fast growing crystal planes (facets) grow out to near extinction and the growing crystal acquires a shape bounded by a small number of the slowest growing facets (28). Further crystal growth is controlled by the growth mechanisms on its bounding slow facets. Similarly, once the loop develops a faceted shape, its further expansion is controlled by the mobility of its two slow facets—the screw and the M111 segments. Given that M111 mobility is the higher of the two, the overall rate of area sweeping by the expanding dislocation loops (and hence the plastic strain rate) is controlled by the mobility of M111 dislocations up to a later time when the loop's aspect ratio grows equal to the mobility ratio of the M111 and the screw orientations. On still further expansion, the two singular orientations should contribute equally to the plastic strain rate and the expanding loop is expected to maintain a constant aspect ratio (see *SI Text* for a more detailed discussion of the rate of loop expansion).

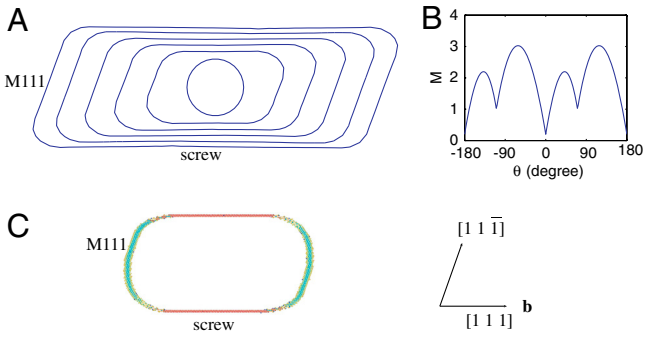

Fig. 6. (*A*) A series of snapshots from a DD simulation of a $\frac{1}{2}[111]$ dislocation loop expanding under stress in the $(1\bar{1}0)$ plane in BCC crystal. (*B*) Dislocation mobility *M* (in arbitrary units) used in this simulation as a function of the line character angle θ. (*C*) MD snapshot of an initially circular dislocation loop expanding in the $(1\bar{1}0)$ plane in Ta under 1 GPa shear stress at 10 K.

Faceting of dislocation lines predicted here for BCC tantalum is a dynamic effect different from a known preference of dislocations to align along certain crystallographic directions in semiconductors (29) and intermetallics (30) where such behaviors have been related to particular core structures and singularly low core energies of dislocations in a few special orientations. We specifically examined for singularities the variations of computed core energy as a function of dislocation character angle but, except for the screw, found none within the FS model used in our calculations. This observation suggests that the M111 facets in BCC Ta are expected to develop only during dislocation motion and are likely to disappear on unloading, because kinks on the M111 dislocations are highly mobile and should quickly reduce to energetically favored rounded shapes as soon as the stress is removed. This behavior is in contrast to the case of silicon where kink mobility is low (29) and dislocation loops retain their faceted shapes long after the stress is removed. The predicted fleeting nature of the M111 facets suggests in situ transmission electron microscopy (TEM) as a means for their observation. Because the kink-pair mechanisms must be rate controlling for the M111 facets to appear, experiments on BCC tantalum must be conducted at low temperature, e.g. $T = 100$ K, see Fig. 5*B*.

The special role of screw dislocations in the plasticity of BCC metals has been well appreciated in large part due to their

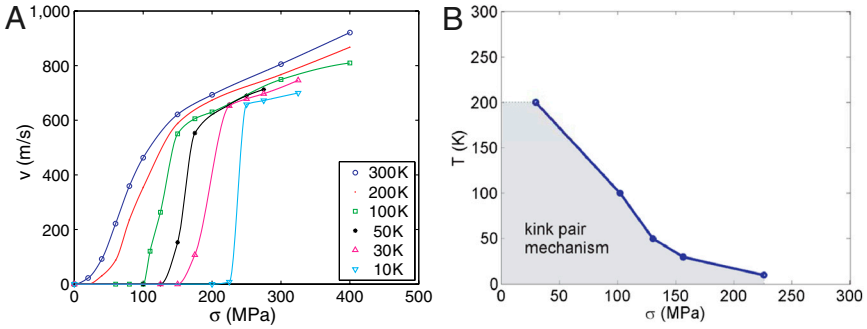

Fig. 5. (*A*) Velocity of the M111 dislocation in BCC Ta as a function of stress at different temperatures. (*B*) The solid line corresponds to temperature and stress conditions at which the dislocation velocity equals 10 m·s^{-1}. The shaded area identifies temperature-stress conditions where the M111 dislocation should move by thermally activated kink mechanism.

exceptionally low mobility. For example, temperature and rate dependence of yield and flow stress in BCC metals have been related, convincingly, to the slow thermally assisted motion of screw dislocations at temperatures below the athermal threshold (25). While confirming the special role of screw dislocations, our calculations show that M111 dislocations, being the second slowest orientation, can also play a special role in low temperature crystal plasticity where the shape and rate of expansion of the dislocation loops should be controlled by their *two slowest* facets. For example, the temperature dependence of the preyield stress (at which the screw dislocations are believed to be sessile) observed in BCC niobium at low temperatures (31) is fully consistent with thermally activated motion of M111 dislocations. We speculate that certain features observed on the yield stress vs. temperature curves in BCC metals in the range of temperatures around 100 K (32, 33) can be attributed to thermally activated kink-pair mechanisms of M111 dislocation motion coming into play at such low temperatures. We conjecture that the yield (or preyield) stress of BCC metals in the zero temperature limit may well be influenced by the PS of the M111 dislocations, instead of being a hallmark of the PS of the screw dislocations as is commonly believed. Thus, the predicted cross-over to kink-pair mechanisms on the M111 dislocations offers a possible explanation for the well known but still unresolved discrepancy between the experimental and theoretical values of the PS: the zero-temperature extrapolation of the critical resolved shear stress at yield for Ta [about 360 MPa (34)] is many times lower than the predicted PS for screw dislocations, but is comparable to the PS of M111 dislocations predicted here. Therefore, whereas existing theories have been focusing on the mobility of screw dislocations, M111 dislocations may be the rate controlling defect in BCC metals at sufficiently low temperatures. We leave it to future work to establish if and how slowing the motion of M111 lines can affect the magnitude of preyield and yield stress in BCC materials at low temperatures. It appears that DD simulations are well suited for the purpose.

Materials and Methods

Molecular Statics Calculation of Peierls Stress. The simulations cells are subjected to periodic boundary conditions along the dislocation line orientation $\boldsymbol{\xi}$ and another orientation **m** (not necessarily orthogonal to $\boldsymbol{\xi}$) on the $(1\bar{1}0)$ slip plane. The free-surface boundary condition is applied in the direction **n** normal to the slip plane. A single dislocation is introduced to the center of the simulation cell using a cut plane normal to $\boldsymbol{\xi} \times \mathbf{n}$. External forces are applied to the surface atoms along the Burgers vector direction **b** to exert shear stress. At each shear stress, the atomic positions are relaxed using the conjugate gradient algorithm. The shear stress is increased in steps of 1 MPa until dislocation motion is observed. The lowest stress at which the dislocation moves by 1 nm is the estimate of the Peierls stress. Simulation cells with different lengths in the **m** and **n** directions (keeping the aspect ratio constant) are used to monitor numerical convergence, while the simulation cell length in the $\boldsymbol{\xi}$ direction is always the minimum lattice repeat distance along that direction.

Molecular Dynamics Simulation of Dislocation Mobility. MD simulations were performed using MD++ (35) and LAMMPS (36) codes with the velocity Verlet algorithm and the integration time step of 1 femtosecond. The temperature was controlled using the Nosé-Hoover thermostat and the shear stress was exerted by applying forces to atoms at the top and at the bottom of the simulation boxes, as described in ref. (37). The methods used to introduce dislocations into the crystal and to extract dislocation velocities were described previously (38).

ACKNOWLEDGMENTS. K.K. and W.C. acknowledge support from the National Science Foundation Grant CMS-0547681. VV.B. acknowledges support of the NNSA ASC Program and the Department of Energy, Basic Energy Sciences, Materials Sciences and Engineering Division. This work was performed under the auspices of the Department of Energy by Lawrence Livermore National Laboratory under Contract W-7405-Eng-48.

1. Taylor GI (1934) Plastic deformation of crystals. *Proc Roy Soc A* 145:362–404.
2. Orowan E (1934) Plasticity of crystals. *Zeit Phys* 89:605–659.
3. Polanyi M (1934) Lattice distortion which originates plastic flow. *Zeit Phys* 89:660–662.
4. Cottrell AH (1953) *Dislocations and Plastic Flow in Crystals* (Clarendon Press, Oxford).
5. Hirth JP, Lothe J (1982) *Theory of Dislocations* (Wiley, New York).
6. Read WT, Shockley W (1950) Dislocation models of crystal grain boundaries. *Phys Rev* 78:275–289.
7. Ackland GJ, Thetford R (1987) An improved N-body semi-empirical model for body-centred cubic transition metals. *Philos Mag A* 56:15–30.
8. Vitek V (1974) Theory of the core structures of dislocations in body-centered cubic metals. *Cryst Latt Def* 5:1–34.
9. Yamaguchi M, Vitek V (1973) Core structure of nonscrew 1/2 ⟨111⟩ dislocations on {110} planes in bcc crystals I. Core structure in an unstressed crystal. *J Phys F Metal Phys* 3:523–536.
10. Peierls R (1940) The size of a dislocation. *Proc Phys Soc* 52:34–43.
11. Nabarro FRN (1947) Dislocations in a simple cubic lattice. *Proc Phys Soc* 59:256–272.
12. Joos B, Duesbery MS (1997) The Peierls stress of dislocations: An analytical formula. *Phys Rev Lett* 78:266–269.
13. Dirichlet Function, Wolfram Mathworld, Wolfram Web Resources, http://mathworld.wolfram.com/DirichletFunction.html.
14. Simmons JP, Rao SI, Dimiduk DM (1997) Atomistics simulations of structures and properties of $\frac{1}{2}$⟨110⟩ dislocations using three different embedded-atom method potentials fit to γ-TiAl. *Philos Mag A* 75:1299–1328.
15. Brailsford AD (1965) Effective line tension of a dislocation. *Phys Rev* 139:A1813–A1817.
16. Cash WD, Cai W (2011) Dislocation contribution to acoustic nonlinearity: The effect of orientation-dependent line energy. *J Appl Phys* 109:014915 Eq. (15).
17. Kelchner CL, Plimpton SJ, Hamilton JC (1998) Dislocation nucleation and defect structure during surface indentation. *Phys Rev B* 58:11085–11088.
18. Honeycutt JD, Andersen HC (1987) Molecular dynamics study of melting and freezing of small Lennard-Jones clusters. *J Phys Chem* 91:4950–4963.
19. Ackland GJ, Jones AP (2006) Applications of local structure measures in experiment and simulation. *Phys Rev B* 73:054104.
20. Abraham FF, Walkup R, Gao H, Duchaineau HM, de La Rubia TD, Seager M (2002) Simulating materials failure by using up to one billion atoms and the world's fastets computer: Work hardening. *Proc Natl Acad Sci USA* 99:5783–5787.
21. Duesbery MS, Xu W (1998) The motion of edge dislocations in body-centered cubic metals. *Script Mater* 39:283287.
22. Chang J, Bulatov VV, Yip S (1999) Molecular dynamics study of edge dislocation motion in a BCC metal. *J Comput-Aided Mater Des* 6:165173.
23. Chang J, Cai W, Bulatov VV, Yip S (2002) Molecular dynamics simulations of motion of edge and screw dislocations in a metal. *Comput Mater Sci* 23:111115.
24. Petukhov BV (1983) Conditions on impurity disordering effects realization in materials. *Fiz Met Metalloved (USSR)* 56:1177–1185.
25. Christian JW, Masters BC (1964) Low-temperature deformation of body-centered cubic metals. *P Roy Soc Lond A Mat* 281:223–257.
26. Marian J, Cai W, Bulatov VV (2004) Dynamic transitions from smooth to rough to twinning in dislocation motion. *Nat Mater* 3:158–163.
27. Terentyev D, Bacon DJ, Osetsky YN (2008) Interaction of an edge dislocation with voids in α-iron modelled with different interatomic potentials. *J Phys Condens Matter* 20:445007.
28. Jackson K (2004) *Kinetic Processes: Crystal Growth, Diffusion and Phase Transitions in Materials* (Wiley-VCH, Weinheim).
29. Nikitenko VI, Eremenko VG (1972) Electron-microscope investigation of microplastic deformation mechanisms in silicon by indentation. *Phys Stat Solidi A* 14:317–330.
30. Balk TJ, Kumar M, Hemker KJ (2001) Influence of Fe substitutions on the deformation behavior and fault energies in Ni3Ge-Fe3Ge L12 intermetallic alloys. *Acta Mater* 49:1725–1736.
31. Boudet A, Kubin LP (1975) Exhaustion mechanisms in the preyield domain of niobium single crystals at low temperatures. *J Phys* 36:823–833.
32. Wasserbach W (1996) Work-hardening and dislocation behavior of tantalum and tantalum alloys. *Proceedings of TMS Meeting* .
33. Kaufmann H-J, Luft A, Schulze D (1984) Deformation mechanism and dislocation structure of high-purity molybdenum single crystals at low temperatures. *Crystal Res Technol* 19:357–372.
34. Takeuchi S, Maeda K (1997) Slip in high purity tantalum between 0.7 and 40 K. *Acta Metall* 25:1485–1490.
35. The MD++ simulation program, http://micro.stanford.edu/MDpp.
36. The LAMMPS simulation program, http://lammps.sandia.gov.
37. Bulatov VV, Cai W (2006) Computer Simulations of Dislocations. (Oxford University Press, Oxford), Chap. 4.
38. Cai W, Li J, Yip S (2012) *Molecular Dynamics*, Comprehensive Nuclear Materials, ed RJM Konings (Elsevier, Amsterdam), 1, pp 249–265.
39. Bulatov VV, Cai W, Baran R, Kang K (2006) Geometric aspects of the ideal shear resistance in simple crystal lattices. *Philos Mag* 86:1–11.